# Spatial Source Phase: A New Feature for Identifying Spatial Differences Based on Complex-Valued Resting-State fMRI Data

**Yue Qiu [1], Qiu-Hua Lin [1, *], Li-Dan Kuang [1], Xiao-Feng Gong [1], Fengyu Cong [2, 3], Yu-Ping Wang [4], and Vince D. Calhoun [5, 6]**

1. *School of Information and Communication Engineering, Faculty of Electronic Information and Electrical Engineering, Dalian University of Technology, Dalian 116024, China*
2. *Department of Biomedical Engineering, Faculty of Electronic Information and Electrical Engineering, Dalian University of Technology, Dalian 116024, China*
3. *Department of Mathematical Information Technology, University of Jyvaskyla, Finland*
4. *Tulane University, New Orleans, Louisiana, USA*
5. *The Mind Research Network, Albuquerque, NM 87106, USA*
6. *Department of Electrical and Computer Engineering, University of New Mexico, Albuquerque, NM 87131, USA*

[*] Corresponding author:

Qiu-Hua Lin, Ph.D.
Professor
School of Information and Communication Engineering
Faculty of Electronic Information and Electrical Engineering
Dalian University of Technology
Dalian 116024, China

Tel.: +86-411-84706697
Fax: +86-411-84706697
Email: qhlin@dlut.edu.cn

# Abstract

Spatial source phase, the phase information of spatial maps extracted from functional magnetic resonance imaging (fMRI) data by data-driven methods such as independent component analysis (ICA), has rarely been studied. While the observed phase has been shown to convey unique brain information, the role of spatial source phase in representing the intrinsic activity of the brain is yet not clear. This study explores the spatial source phase for identifying spatial differences between patients with schizophrenia (SZs) and healthy controls (HCs) using complex-valued resting-state fMRI data from 82 individuals. ICA is first applied to preprocess fMRI data, and post-ICA phase de-ambiguity and denoising are then performed. The ability of spatial source phase to characterize spatial differences is examined by the homogeneity of variance test (voxel-wise *F*-test) with false discovery rate correction. Resampling techniques are performed to ensure that the observations are significant and reliable. We focus on two components of interest widely used in analyzing SZs, including the default mode network (DMN) and auditory cortex. Results show that the spatial source phase exhibits more significant variance changes and higher sensitivity to the spatial differences between SZs and HCs in the anterior areas of DMN and the left auditory cortex, compared to the magnitude of spatial activations. Our findings show that the spatial source phase can potentially serve as a new brain imaging biomarker and provide a novel perspective on differences in SZs compared to HCs, consistent with but extending previous work showing increased variability in patient data.



**Keywords:** Spatial source phase; Complex-valued fMRI data; Resting-state fMRI data; Independent component analysis; Default mode network; Auditory cortex; Schizophrenia.

# 1. Introduction

Functional magnetic resonance imaging (fMRI) is a neuroimaging technique based on the blood-oxygenation-level-dependent (BOLD) effect attributed to neuronal activity (Ogawa et al., 1990). The non-invasiveness and high spatial resolution make it to be employed in a wide range of areas such as basic neuroscience research and clinical imaging (Belliveau et al., 1991; Stippich, 2008). fMRI has provided valuable insights on understanding how human brain functions and how the disease disrupts healthy brain activity (He et al., 2009; Grossman et al., 2013). Independent component analysis (ICA) is a widely-used data-driven blind source separation technique for recovering a set of maximally independent sources from their observed data. The advantages of no need for knowledge of the source signals and the mixing parameters make it possible to find differential activation patterns (also called spatial maps, SMs) at different brain locations and their associated time courses (TCs) from fMRI data (Mckeown et al., 1998; Calhoun et al., 2002; Calhoun and Adalı, 2012b). Consequently, ICA has contributed greatly to the further understanding of intrinsic brain networks and functional connectivity at the network level by using SMs and TCs, respectively (Jafri et al., 2008; Calhoun and Adalı, 2012b; Arbabshirani et al., 2013).

Although fMRI data is initially acquired as a bivariate complex image pair including magnitude and phase images (Adalı and Calhoun, 2007; Rowe et al., 2007; Calhoun and Adalı, 2012a; Hagberg and Tuzzi, 2014; Adrian et al., 2018), the vast majority of fMRI data analysis focuses on magnitude data due to the noisy characteristic of phase data. However, a growing body of work suggests that the phase data conveys physiologic information about brain functionality that is not captured by magnitude-only data (Hoogenraad et al., 1998; Menon, 2002; Nencka and Rowe, 2007; Tomasi and Caparelli, 2007; Arja et al., 2010; Curtis et al., 2014; Hagberg and Tuzzi, 2014; Chen and Calhoun, 2016). For example, Hoogenraad et al. observed that phase values within functional activated areas reflect unequal oxygenation levels of blood, showing activation-dependent changes (Hoogenraad et al., 1998), and Arja et al. found phase changes in response to event stimuli for multiple types of fMRI tasks (Arja et al., 2010). Menon suggested that the phase is related in part to the oriented macrovascular and demonstrated that it is possible to identify and remove unwanted

macrovascular contributions based on phase shifts (Menon, 2002), consistent with subsequent findings (Tomasi and Caparelli, 2007; Curtis et al., 2014). Recently, Chen et al. performed group ICA and functional network connectivity on phase fMRI data and illustrated that phase data can be used to identify resting-state networks consistent with while not identical to those identified from magnitude data and exhibiting different inter-network connectivity patterns (Chen et al., 2018). In addition, Adrian et al. provided detailed and comprehensive evaluation of the benefits of using both magnitude and phase information in fMRI (Adrian et al., 2018). Multiple publications have provided evidences that phase data plays a complementary role to magnitude data in extracting contiguous and meaningful brain activations (Rodriguez et al., 2011, 2012; Yu et al., 2015; Kuang et al., 2017a, 2017b). Moreover, the incorporation of fMRI phase data better preserves the integrity of larger networks (Kuang et al., 2017a, 2018), and the intact group default mode network (DMN) at higher model orders shows significant difference between patients with schizophrenia (SZs) and healthy controls (HCs) (Kuang et al., 2018).

From the above review, it is obvious that most previous research on fMRI phase data focused on the observed phase data directly collected from the MRI scan. The observed phase contains not only components related to brain activities but also physiological noise. The spatial source phase, the phase information of the SMs separated by spatial ICA, is largely denoised compared to the observed phase, which is an efficient way to identify and suppress unwanted voxels (Yu et al., 2015). However, it is unknown to what degree the spatial source phase conveys unique information in exhibiting the intrinsic activity of the brain. We propose applying the spatial source phase of resting-state complex-valued fMRI data separately to distinguish SZs from HCs, because the observed phase has been shown to improve the classification of SZs and HCs as mentioned earlier (Castro et al., 2014). Note that abundant evidence of neuroanatomical variability has been found in resting-state networks (RSNs) such as the DMN and auditory cortex of SZs from previous studies (Pearlson et al., 1997; Olabi et al., 2011; Padmanabhan et al., 2015; Sui et al., 2015), which provides a physiological basis for the study of spatial activation variability in schizophrenia. Gopal et al. have found significantly increased voxel amplitude variance in the SMs for the auditory cortex, basal

ganglia, sensorimotor network and visual cortex of SZs (Gopal et al., 2015). Motivated by this spatial activation variability seen in magnitude-only fMRI data, we investigate voxel-wise differences contained within the variance of spatial source phase and define the variance difference index, in order to evaluate the potential of spatial source phase as a brain imaging biomarker.

In this study, we explore the spatial source phase characteristics based on resting-state complex-valued fMRI data from 82 individuals (42 SZs and 40 HCs). Complex-valued ICA is employed to extract SM estimates from fMRI data. The DMN and auditory cortex are selected as components of interest. Phase de-ambiguity based on TC estimates (Yu et al., 2015) is first employed to adjust the SM phase for correctly representing the spatial source phase changes of all voxels under severe noise conditions. Phase denoising is then used to remove the noisy voxels from SM estimates. Voxel-wise variance maps of each component of interest are generated for each group (SZs or HCs) by estimating the variance of each voxel across each group. We perform a homogeneity of variance test (voxel-wise *F*-test) to identify spatial differences between SZs and HCs, and the *p*-values of *F*-test are corrected for multiple comparison using a false discovery rate (FDR) correction. Finally, resampling techniques are used to validate the significance of group differences.

# 2. Materials and Methods

## 2.1 Materials

The fMRI datasets used in this study have been described in Kuang et al. (2018). Resting-state complex-valued fMRI data were collected from 40 HCs and 42 SZs with written subject consent overseen by the University of New Mexico Institutional Review Board. During the scan, all subjects were instructed to rest quietly in the scanner, keep their eyes open without sleeping and not to think of anything in particular. FMRI scans were acquired using a 3.0 Tesla Siemens Allegra scanner, equipped with 40 mT/m gradients and a standard quadrature head coil. The functional scan was acquired using gradient-echo echo-planar imaging with the following parameters: TR = 2 s, TE = 29 ms, field of view = 24 cm, acquisition matrix =

64 × 64, flip angle =75°, slice thickness = 3.5 mm, slice gap = 1 mm. Data preprocessing was performed using the SPM software package (available at http://www.fil.ion.ucl.ac.uk/spm). Five scans were excluded due to steady state magnetization effects. Functional images were motion corrected and then spatially normalized into the standard Montreal Neurological Institute space. Following spatial normalization, the data were slightly sub-sampled to 3 × 3 × 3 mm³, resulting in 53 × 63 × 46 voxels. Both magnitude and phase images were spatially smoothed with an 8 × 8 × 8 mm³ full width half-maximum (FWHM) Gaussian kernel. Phase images were first motion corrected using the transformations computed from magnitude-only data; next, complex division of phase data by the first time point reduced the need for phase unwrapping; and spatial normalization of phase images used the warp parameters computed from magnitude-only data. A total of 146 scans (i.e., time points) per subject were entered into the ICA analysis.

## 2.2 ICA separation and component selection

Given the observed fMRI data of a single-subject $\mathbf{X}^k \in \mathbb{C}^{T\times V}$ ($k = 1,\ldots,K$), where $T$ is the total number of time points, $V$ is the number of in-brain voxels, and $K$ denotes the number of subjects. We use a higher number of components $N$ = 120 since ICA with a larger model order can provide more detailed evaluation of RSNs (Abou-Elseoud et al., 2010; Allen et al., 2011). For subject $k$, the model of ICA is $\mathbf{X}^k = \mathbf{A}^k\mathbf{S}^k$, where $\mathbf{A}^k = \{\mathbf{a}_n^k\} \in \mathbb{C}^{T\times N}$ and $\mathbf{S}^k = \{\mathbf{s}_n^k\} \in \mathbb{C}^{N\times V}$ ($n = 1,\ldots,N$) denote TC and SM estimates. We adopt the entropy bound minimization (EBM) algorithm (Li and Adalı, 2010), an efficient complex-valued ICA algorithm, for component separation, and repeat the ICA separation $R$ (here $R$ = 10) times.

Two components of interest, the DMN and auditory cortex, are identified from $N$ components of each run based on spatial reference networks detected in Smith et al. (2009) (Fig. 1(1)) and Allen et al. (2011) (Fig. 2(1)). The component of interest for subject $k$ at run $r$ ($r = 1,\ldots,R$) is selected using the following criterion:

$$c^* = \arg\max_{c=1,\ldots,C} \left( \frac{\mathbf{s}_{c,r}^k \cap \mathbf{s}_{\text{ref}}}{\mathbf{s}_{\text{ref}}} \cdot \frac{\mathbf{s}_{c,r}^k \cap \mathbf{s}_{\text{ref}}}{\mathbf{s}_{c,r}^k} \right), \quad (1)$$

where $\mathbf{s}_{\text{ref}}$ is the spatial reference, $\mathbf{s}_{c,r}^k$, $c=1,\ldots,C$, denote $C$ candidate components at run $r$ with top $C$ correlation coefficients with $\mathbf{s}_{\text{ref}}$ (e.g., $C$ = 10), "$\cap$" denotes the number of voxels activated in both $\mathbf{s}_{c,r}^k$ and $\mathbf{s}_{\text{ref}}$, and activated voxels are those with magnitude larger than 0.5 as used in Yu et al. (2015). Eq. (1) aims to select a component with more voxels inside the spatial reference network as well as less voxels outside the spatial reference network. For simplicity, we denote the selected SM estimate and associated TC estimate for subject $k$ at run $r$ as $\mathbf{s}_r^k$ and $\mathbf{a}_r^k$.

## 2.3 Post-ICA processing for spatial source phase

We first performed spatial source phase preprocessing on selected components $\mathbf{s}_r^k$ ($k=1,\ldots,K$, $r=1,\ldots,R$) including phase de-ambiguity and denoising using the method proposed in Yu et al. (2015). The phase correction angle $\theta_r^k$ is calculated by maximizing the energy of the TC real part:

$$\theta_r^k = \arg\max_{\theta_r^k} \sum_{t=1}^{T} (\text{Re}\{a_{r,t}^k e^{-j\theta_r^k}\})^2, \tag{2}$$

where $a_{r,t}^k$ is the element of $\mathbf{a}_r^k$, "Re{·}" denotes the real part. Rotating $\mathbf{s}_r^k$ by $\theta_r^k$ and removing the sign ambiguity based on the correlation of rotated SM estimate and the spatial reference, we obtain the SM component $\underline{\mathbf{s}}_r^k$ without spatial source phase ambiguity:

$$\underline{\mathbf{s}}_r^k = \begin{cases} (-1)\cdot e^{j\theta_r^k}\mathbf{s}_r^k, & \text{if } \text{corr}\left(\text{Re}\{e^{j\theta_r^k}\mathbf{s}_r^k\}, \mathbf{s}_{\text{ref}}\right) < 0 \\ e^{j\theta_r^k}\mathbf{s}_r^k, & \text{otherwise} \end{cases} \tag{3}$$

where "corr(·)" denotes the correlation coefficient between two vectors, and '-1' rotates $\mathbf{s}_r^k$ by 180 degrees in the complex domain.

Phase denoising classifies the whole voxels of $\underline{\mathbf{s}}_r^k$ into two categories according to their spatial source

phase values. BOLD-related voxels are located within small phase range $[-\pi/4, \pi/4]$, and others are regarded as unwanted voxels. The efficiency of $[-\pi/4, \pi/4]$ has been verified for both task (Yu et al., 2015) and resting (Kuang et al., 2017b) fMRI data. We also ignore voxels with very small magnitude. Thus, we define a single-subject mask for subject *k* at run *r*:

$$b_{r,v}^{k} = \begin{cases} 1, & \text{if } \underline{s}_{r,p}^{k}(v) \in [-\pi/4, \pi/4] \text{ and } \underline{s}_{r,m}^{k}(v) > Z_{\text{th}} \\ 0, & \text{otherwise} \end{cases} \tag{4}$$

where $\underline{s}_{r,p}^{k}(v)$ and $\underline{s}_{r,m}^{k}(v)$ denote phase and magnitude values of the voxel $v$ ($v = 1, \ldots, V$) in $\underline{\mathbf{s}}_{r}^{k}$, respectively. Here, $Z_{\text{th}}$ is set to 0.5 (Yu et al., 2015) and $\mathbf{b}_{r}^{k} = \{b_{r,v}^{k}\} \in \mathbb{R}^{V}$ is a binary mask for denoising. We get the denoised SM estimate for subject *k* at run *r* as follows:

$$\underline{\mathbf{s}}_{r,*}^{k} = \underline{\mathbf{s}}_{r}^{k} \circ \mathbf{b}_{r}^{k}, \tag{5}$$

where "$\circ$" means the Hadamard product.

We next select the best run of $\underline{\mathbf{s}}_{r,*}^{k}$ from all *R* runs ($r = 1, \ldots, R$) for subject *k* using the approach proposed in Kuang et al. (2018):

$$r^{*} = \arg\max_{r=1,\ldots,R} |\operatorname{corr}(\underline{\mathbf{s}}_{r,*}^{k}, \mathbf{s}_{\text{ref}}^{k})|, \tag{6}$$

where "$|\cdot|$" denotes the magnitude calculation, $\mathbf{s}_{\text{ref}}^{k} = \{s_{\text{ref}}^{k}(v)\} \in \mathbb{R}^{V}$ is a reference generated by combining cross-run averaging and a one-sample *t*-test:

$$s_{\text{ref}}^{k}(v) = \begin{cases} [\underline{s}_{1,*}^{k}(v) + \ldots + \underline{s}_{R,*}^{k}(v)]/R, & \text{if } \text{p\_ttest}(\underline{s}_{1,*}^{k}(v), \ldots, \underline{s}_{R,*}^{k}(v)) < p_{\text{th}} \\ 0, & \text{otherwise} \end{cases}, \tag{7}$$

p_ttest(·) denotes the *p*-value of the one-sample *t*-test, and $p_{\text{th}}$ is a *p*-value threshold ($p_{\text{th}} = 0.05$).

Finally, we define a group mask $\tilde{\mathbf{b}} = \{\tilde{b}_{v}\} \in \mathbb{R}^{V}$ based on the individual masks, given in Eq. (4), at the best

runs to extract shared activated voxels in all subjects for group analysis, and

$$\tilde{b}_v = \begin{cases} 1, & \text{if } \sum_{k=1}^{K} b_{r^*,v}^k \geq \frac{K}{2} \\ 0, & \text{otherwise} \end{cases} \tag{8}$$

Masking the phase corrected SM estimates, referring to Eq. (3), at the best runs by the group mask, we obtain the denoised single-subject SM estimate:

$$\underline{\mathbf{s}}_*^k = \underline{\mathbf{s}}_{r^*}^k \circ \tilde{\mathbf{b}} \tag{9}$$

The phase of $\underline{\mathbf{s}}_*^k$, denoted as $\boldsymbol{\varphi}^k$, is the spatial source phase that we utilize for further analysis.

## 2.4 Voxel-wise differences in variance for SZs and HCs

Assuming the number of non-zero elements in the group mask $\tilde{\mathbf{b}}$ is *M*, we have $\boldsymbol{\varphi}^k = \{\varphi_i^k\} \in \mathbb{R}^M$, $i = 1,\ldots,M$, where $\varphi_i^k$ corresponds to the spatial source phase value of voxel *i* in $\underline{\mathbf{s}}_*^k$. Next, we denote the spatial source phase values of voxel *i* across total *K* subjects as a vector $\boldsymbol{\varphi}_i = \{\varphi_i^k\} \in \mathbb{R}^K$ ($k = 1,\ldots,K$ and $i = 1,\ldots,M$), and describe the voxel-wise spatial source phase vectors for SZs and HCs as $\boldsymbol{\varphi}_i^{\text{SZ}} \in \mathbb{R}^{K_1}$ and $\boldsymbol{\varphi}_i^{\text{HC}} \in \mathbb{R}^{K_2}$, where $K_1$ and $K_2$ denote the numbers of SZs and HCs, respectively ($K_1$ = 42 and $K_2$ = 40). Then, we perform a voxel-wise *F*-test (with and without FDR correction of 0.05) on $\boldsymbol{\varphi}_i^{\text{SZ}}$ and $\boldsymbol{\varphi}_i^{\text{HC}}$, and generate voxel-wise SZ-HC difference variance maps:

$$d_{i,\text{SZ-HC}}^* = \begin{cases} \text{var}(\boldsymbol{\varphi}_i^{\text{SZ}}) - \text{var}(\boldsymbol{\varphi}_i^{\text{HC}}), & \text{if } \text{p\_ftest}(\boldsymbol{\varphi}_i^{\text{SZ}}, \boldsymbol{\varphi}_i^{\text{HC}}) < p_{\text{th}} \\ 0, & \text{otherwise} \end{cases} \tag{10}$$

where "$\text{var}(\cdot)$" denotes the variance of a vector, "$\text{p\_ftest}(\cdot)$" denotes the *p*-value of the voxel-wise *F*-test. The nonzero elements in $\mathbf{d}_{\text{SZ-HC}}^* = \{d_{i,\text{SZ-HC}}^*\} \in \mathbb{R}^M$ denote voxels with significantly different variance of spatial source phase between SZs and HCs, and positive values mean voxels with higher variance in SZs

versus HCs. Let the number of non-zero elements in $\mathbf{d}^{*}_{\text{SZ-HC}}$ be $m_*$, the numbers of positive and negative elements be $m_*^{\text{SZ}}$ and $m_*^{\text{HC}}$, $m_* = m_*^{\text{SZ}} + m_*^{\text{HC}}$. We define $q^* = m_*^{\text{SZ}} / m_*$ ($q^* \in [0,1]$) as an unsigned variance difference index for performing validation of one sample *t*-test, and transform it to a signed variance difference index $q^{*}_{\text{SZ-HC}} \in [-1,1]$ to show that which group experiences more changes:

$$q^{*}_{\text{SZ-HC}} = \begin{cases} q^*, & \text{if} \quad q^* \geq 0.5 \\ q^* - 1, & \text{otherwise} \end{cases}. \tag{11}$$

$q^{*}_{\text{SZ-HC}} > 0$ means that SZs experience more changes among subjects than HCs, and vice versa. The higher the absolute value of $q^{*}_{\text{SZ-HC}}$ is, the greater the differences between SZs and HCs are. We record $m_* > 200$ together with $|q^{*}_{\text{SZ-HC}}| \geq 0.8$ as a significant difference between SZs and HCs in order to obtain consistent results for actual and resampling data, and predict that SZs will show larger variance than HCs for the spatial source phase. A detailed procedure for the proposed method to analyze the spatial source phase is described in Table I.

## 2.5 Validation of Results

We use a bootstrap resampling technique to determine whether the variance difference of spatial source phase between SZs and HCs is significant. We generate 1000 bootstrap samples of 82 subjects and re-compute the variance difference indexes $q^*$ using steps 7-9 in Table I for the relabeled SZs and HCs, to build a null distribution. We then use the bias-corrected and accelerated (BCa) method (Efron and Tibshirani, 1993) to obtain the associated *p*-value for the single variance difference of actual groups.

In addition, it is reasonable to ask whether the differences we found are related to the instability of spatial source phase. To address this, we utilize a resampling approach to evaluate the results, as described in Table II. The detailed implementations are carried out in two sub-groups of subjects, namely G1 and G2. There is no identical subject among them, and each sub-group is assumed to include $K'$ subjects (here

$K' = 20$). The composition of two sub-groups G1 and G2 consists of three cases: (1) G1 and G2 both correspond to SZs to measure intra-SZ differences. (2) G1 and G2 both correspond to HCs to measure intra-HC differences. (3) G1 corresponds to SZs and G2 corresponds to HCs to measure inter-group differences. The selection of G1 and G2 in the three cases is random and repeated *L* times to form *L* trials (here *L* = 1000). Let $\boldsymbol{\varphi}_i^{[l,\mathrm{G1}]}$ and $\boldsymbol{\varphi}_i^{[l,\mathrm{G2}]}$ denote the spatial source phase vectors of voxel *i* for G1 and G2 in trial *l*, $l = 1,\ldots,L$. We perform a voxel-wise *F*-test (with and without FDR correction of 0.05) on $\boldsymbol{\varphi}_i^{[l,\mathrm{G1}]}$ and $\boldsymbol{\varphi}_i^{[l,\mathrm{G2}]}$, and detect voxels with significantly different variance of spatial source phase between G1 and G2 in trial *l*:

$$d_{i,\mathrm{G1\text{-}G2}}^{[l,*]} = \begin{cases} \mathrm{var}\,(\boldsymbol{\varphi}_i^{[l,\mathrm{G1}]}) - \mathrm{var}\,(\boldsymbol{\varphi}_i^{[l,\mathrm{G2}]}), & \text{if } \mathrm{p\_ftest}\,(\boldsymbol{\varphi}_i^{[l,\mathrm{G1}]},\ \boldsymbol{\varphi}_i^{[l,\mathrm{G2}]}) < p_{\mathrm{th}} \\ 0, & \text{otherwise} \end{cases} \tag{12}$$

Assuming that $m_*^l$ denotes the number of nonzero elements in $\mathbf{d}_{\mathrm{G1\text{-}G2}}^{[l,*]} = \{d_{i,\mathrm{G1\text{-}G2}}^{[l,*]}\} \in \mathbb{R}^M$, and $m_*^{[l,\mathrm{G1}]}$ and $m_*^{[l,\mathrm{G2}]}$ denote the numbers of voxels which have larger variance in G1 and G2, respectively, then $m_*^l = m_*^{[l,\mathrm{G1}]} + m_*^{[l,\mathrm{G2}]}$ and $m_*^{\mathrm{G}} = (\sum_{l=1}^{L} m_*^l)/L$ denotes the average number of voxels showing significant differences between G1 and G2 across *L* trials. We define an unsigned variance difference index $q_{\mathrm{G}}^{[l,*]} = m_*^{[l,\mathrm{G1}]} / m_*^l$ to identify significant group differences between G1 and G2 in trial *l*, in order to enable calculations of $\bar{q}_{\mathrm{G}}^* = (\sum_{l=1}^{L} q_{\mathrm{G}}^{[l,*]})/L$ (i.e., the mean) and the standard deviation of $q_{\mathrm{G}}^{[l,*]}$ across *L* trials. The unsigned $\bar{q}_{\mathrm{G}}^*$ is transformed into a signed variance difference index $q_{\mathrm{G1\text{-}G2}}^*$, as defined in Eq. (11):

$$q_{\mathrm{G1\text{-}G2}}^* = \begin{cases} \bar{q}_{\mathrm{G}}^*, & \text{if } \bar{q}_{\mathrm{G}}^* \geq 0.5 \\ \bar{q}_{\mathrm{G}}^* - 1, & \text{otherwise} \end{cases} \tag{13}$$

The higher the absolute value of $q_{\mathrm{G1\text{-}G2}}^*$ is, the greater the differences between G1 and G2 are. We predict that the absolute values of $q_{\mathrm{G1\text{-}G2}}^*$ in case (1) and (2) would be about the same (about 0.5) but be large in

case (3), indicating larger inter-group variance differences.

# 3. Results

## 3.1 Component selection and spatial source phase processing

Fig. 1 and Fig. 2 show the maps for the DMN and auditory cortex from SZs and HCs after ICA and post-ICA processing (see step 1 to step 6 in Table I). Fig. 1 displays results for the DMN. The correlation coefficients between the spatial reference shown in Fig. 1(1) and the SM estimates at the best run are 0.72 ± 0.06 (mean ± standard deviation) for all subjects. The number of shared activated voxels for all subjects is 6795 under the group mask shown in Fig. 1(2). Figs. 1(3) and 1(4) show the group magnitude and spatial source phase maps, which were generated by averaging single-subject magnitude and spatial source phase maps across SZs and HCs, respectively. We observe that the group magnitude maps, as shown in Fig. 1(3A) and Fig. 1(3B), are more similar between SZs and HCs (correlation coefficient of 0.98), whereas the group spatial source phase maps exhibit large spatial differences (correlation coefficient of 0.06), as shown in Figs. 1(4A) and 1(4B).

Fig. 2 shows a comparison of the maps for the auditory cortex. The correlation coefficients between the spatial reference shown in Fig. 2(1) and the SM estimates at the best run are 0.71 ± 0.11 (mean ± standard deviation) for all subjects. Fig. 2(2) is the group mask with shared activated voxels of 5037. Fig. 2(3) and Fig. 2(4) display the group magnitude and spatial source phase maps for SZs and HCs. The group magnitude maps, as shown in Fig. 2(3A) and Fig. 2(3B), also illustrate more similar activations between SZs and HCs (correlation coefficient of 0.98), as demonstrated for the DMN component. Regarding the spatial source phase maps, the differences between SZs and HCs are still large (correlation coefficient of 0.21), as shown in Fig. 2(4A) and Fig. 2(4B).

## 3.2 Voxel-wise differences in variance for SZs and HCs

To confirm the discrimination on schizophrenia, we compared the spatial source phase with the magnitude

in terms of voxel-wise difference variance maps between SZs and HCs (see step 7 to step 9 in Table I). Figs. 3 and 4 are the results for the DMN and auditory cortex. Figs. 3(1A) and 3(2A) are the variance maps of SZs from the magnitude and spatial source phase, while the variance maps of HCs are displayed in Figs. 3(1B) and 3(2B). Fig. 3(C) to Fig. 3(E) show the difference variance maps of SZ-HC obtained from the magnitude and spatial source phase without the voxel-wise *F*-test, with the voxel-wise *F*-test at $p < 0.05$ without and with FDR correction, respectively. Red and yellow voxels denote increased variance in SZs versus HCs, while blue voxels represent increased variance in HCs versus SZs. We observe from Figs. 3(D) and 3(E) that more differences in the spatial source phase maps successfully survived the voxel-wise *F*-test (2832 vs. 642) and the voxel-wise *F*-test with FDR correction (2744 vs. 9) than the magnitude maps. In other words, 96.9% significant voxels passed FDR correction for spatial source phase maps but 1.4% for magnitude maps. The spatial source phase maps exhibited increased variance clusters in the anterior cingulate cortex (ACC) for SZs versus HCs, as shown in Fig. 5(A).

Fig. 4 includes difference variance maps for the auditory cortex. Similar to the DMN results above, the spatial source phase maps included more contiguous significant voxels than the magnitude maps (1843 vs. 1101), as demonstrated in Fig. 4(D). In addition, the number of significant voxels passing FDR correction was 1641 (89.0%) for the spatial source phase maps, but was 355 (32.2%) for the magnitude maps, as shown in Fig. 4(E). The spatial source phase showed increased variance clusters in the left part of auditory cortex (AL) for SZs versus HCs, as shown in Fig. 5(B).

To further explore the detailed spatial activation variability, we examined the sub-networks of the DMN and auditory cortex. The DMN contains three parts corresponding to ACC, the posterior cingulate cortex (PCC), and inferior parietal lobule (IPL) respectively (see Fig. 1(1)), while the auditory cortex can be split into the AL and the right part of auditory cortex (AR) according to Fig. 2(1). Fig. 6 shows the number of significant voxels $m_*$ that survived the voxel-wise *F*-test at $p < 0.05$ (with and without FDR correction of 0.05) and the difference variance index $q^*_{\text{SZ-HC}}$ for sub-networks of DMN and auditory cortex. Note $q^*_{\text{SZ-HC}}$

was calculated only when $m_* > 200$ with the purpose of taking more voxels into the computation. The difference satisfying both $m_* > 200$ and $|q^*_{\text{SZ-HC}}| \geq 0.8$ is regarded as a signicant difference. It is observed that more significant voxels were detected by the spatial source phase than the magnitude for all sub-networks, and more voxels in the spatial source phase maps passed FDR correction than the magnitude maps. Spatial source phase maps detected significant network variability (SZs are greater than HCs) in both the ACC and the AL with (ACC: $q^*_{\text{SZ-HC}} = 1$; AL: $q^*_{\text{SZ-HC}} = 0.97$) and without (ACC: $q^*_{\text{SZ-HC}} = 1$; AL: $q^*_{\text{SZ-HC}} = 0.96$) FDR correction. In contrast, magnitude maps detected significant variability in the AR (SZs are greater than HCs, and $q^*_{\text{SZ-HC}} = 0.81$), but failed to pass FDR correction.

## 3.3 Validation of Results

Table III records the results of variance difference validation using bootstrap sampling. We calculate the *p*-values on unsigned values $q^*$ and provide $m_*$ for determining whether the difference is significant. We observe that the variance differences in all sub-networks except PCC are significantly different from the relabeled data ($p < 0.04$). Among others, the ACC ($p < 1.0 \times 10^{-35}$) and AL ($p < 1.0 \times 10^{-9}$) satisfy both $m_* > 200$ and $|q^*_{\text{SZ-HC}}| \geq 0.8$.

Figs. 7 and 8 show the validation results of the average intra-SZ, intra-HC and inter-group differences in the sub-networks of DMN and auditory cortex in terms of the number of significant voxels ($m^{\text{G}}_*$) and mean variance difference index $q^*_{\text{G1-G2}}$. The magnitude maps showed more significant voxels than the spatial source phase maps in the ACC when measuring intra-SZ differences, but this finding failed to pass FDR correction, see Fig. 7(A). In contrast, with and without FDR correction, the spatial source phase maps both exhibited much more significant voxels than the magnitude maps in the PCC, IPL, AL and AR for all three cases, see Figs. 7(A) and 8(A). However, when considering $m^{\text{G}}_*$ together with $q^*_{\text{G1-G2}}$ for the results from the spatial source phase maps, the intra-SZ and intra-HC differences were not consistent across *L* trials,

while the inter-group differences displayed great consistency. More precisely, the intra-SZ and intra-HC $q^*_{\text{G1-G2}}$ values in each region were about 0.5, as shown in Figs. 7(B) and 8(B), thus it is hard to determine the bigger intra-SZ and intra-HC variance differences from G1 and G2. On the contrary, $m^{\text{G}}_* > 200$ and $|q^*_{\text{G1-G2}}| \geq 0.8$ were satisfied in the ACC and AL regions when detecting the inter-group differences. The spatial source phase variances of SZs are greater than HCs for both the ACC ($q^*_{\text{G1-G2}} = 0.97$ without and with FDR correction) and the AL ($q^*_{\text{G1-G2}} = 0.84$ and $q^*_{\text{G1-G2}} = 0.85$ without and with FDR correction). These results support the SZ-HC differences detected in Figs. 3 to 6. In addition, it is observed from Figs. 7(B) and 8(B) that standard deviations of inter-group differences were smaller than those of intra-group differences, indicating that the intra-group differences are more influenced by the selection of subjects, while the inter-group differences are relatively stable.

# 4. Discussion

To our knowledge, few studies have evaluated the spatial source phase maps obtained by complex-valued ICA. In this study, we proposed investigating the potential of spatial source phase and explore its role in representing the intrinsic activity of the brain. We concentrated on the variation of spatial source phase for identifying SZs. The resting-state complex-valued fMRI data were used and the homogeneity of variance test (voxel-wise *F*-test) with FDR correction was performed. We selected the DMN and auditory cortex as components of interest and further investigated the spatial differences between SZs and HCs in their sub-networks. Spatial source phase maps showed greater discrimination, higher sensitivity and more reliability in identifying SZs, compared with magnitude maps. Among others, the ACC and AL demonstrated much higher spatial source phase variation in SZs. The resampling techniques further confirmed the robustness of the findings. In summary, the spatial source phase may prove useful in shedding light on pathogenesis of schizophrenia and serve as a new biomarker for the identification of diseases.

The spatial source phase was obtained from ICA of complex-valued fMRI data with phase preprocessing. Although the best run selection for ICA is based on magnitude data (Kuang et al., 2018), both the magnitude

maps and spatial source phase maps show variability across different runs of ICA and the selected magnitude and spatial source phase maps appear more than half of *R* runs. This further illustrates the stability of the results for ICA and the effectiveness of the best run selection for both magnitude maps and spatial source phase maps. The phase de-ambiguity guarantees that phase values of voxels in the activated regions are concentrated near zero degrees and phase denoising further removed voxels with large phase values, giving rise to the spatial source phase with small values and relative to zero symmetry. Thus, we used *F* statistic to evaluate the difference on the variance of spatial source phase maps between SZs and HCs.

Broad comparability exists between the spatial source phase and the observed phase. The spatial source phase had similar denoising ability with the observed phase in that spatial source phase can identify about 60 – 70% unwanted voxels (Yu et al., 2015), which is comparable to the desired range of the observed phase changes accounting for about 25 – 34% of the full phase changes (Menon, 2002; Tomasi and Caparelli, 2007). In this study, spatial source phase conveyed additional brain information beyond the magnitude, while the observed phase changes captured unique physiologic information that was not observable in the magnitude data (Hoogenraad et al., 1998; Menon, 2002; Nencka and Rowe, 2007; Tomasi and Caparelli, 2007; Arja et al., 2010; Curtis et al., 2014; Hagberg and Tuzzi, 2014; Chen and Calhoun, 2016). What's more, the spatial source phase showed higher sensitivity for spatial variability and detected many more significant voxels in the difference variance maps, as compared with the magnitude, supporting the finding that the observed phase showed greater spatial variation than the magnitude at higher spatial resolution (Chen and Calhoun, 2010). The increase in sensitivity of the source phase in identifying group differences may be due to a fingerprint characteristic which is supported by the observed phase (Hagberg and Tuzzi, 2014). The significant increase in sensitivity on spatial variability and detected voxels would increase the reliability of the source phase in identifying diseases as a new biomarker; the significant inter-group differences versus insignificant intra-group differences indicate that the spatial source phase conveys unique and representative information of groups. These reinforce the notion that the phase data indeed provide

reliable information to better characterize schizophrenia (Castro et al., 2014). Additionally, the spatial source phase can be an efficient and reliable complement of the magnitude for identifying spatial differences, similar to the fact that the observed phase of the BOLD signal is complementary to its magnitude. Since the magnitude and spatial source phase have different ranges of values (magnitude: larger than 0.5; spatial source phase: $[-\pi/4, \pi/4]$ ) and they are nonlinear related, the complementary relationship of the spatial source phase and the magnitude can be various. Similar or dissimilar difference variance for the magnitude and spatial source phase maps is possible and reasonable. Along this line, devising a composite variance marker that includes both magnitude and phase would ultimately be the goal, but it is a challenging problem beyond the scope of this study.

The DMN and auditory cortex were selected as components of interest since wide-spread differences have been observed in these two RSNs of SZs (Calhoun et al., 2008, 2009; Gopal et al., 2015). It has been demonstrated that there are abnormal functional activities within DMN of patients with schizophrenia (Garrity et al., 2007; Harrison et al., 2007; Whitfield-Gabrieli et al., 2009; Jeong et al., 2010; Mannell et al., 2010). Using the resting-state complex-valued fMRI data from 82 individuals, we found that most voxels in the ACC of SZs have larger variance of spatial source phase than HCs, as shown in Fig. 3, Figs. 5-7, and Table III. Voxels in the ACC of SZs having substantially higher variance is related to previous studies, which stated abnormal fMRI activation of the ACC plays a role in the positive symptoms of schizophrenia (Fletcher et al., 1999). Abnormality in the function of bilateral temporal lobe including the auditory cortex is also a prominent feature of schizophrenia (Anderson et al. 2002; Calhoun et al., 2004; Sweet et al., 2008; Gopal et al., 2015). According to Figs. 4-6, Fig. 8, and Table III, our results on spatial source phase showed higher variance in the AL of SZs than HCs. This finding is supported by the results of structural MRI data from Pearlson et al. (1997) showing differences between SZs and HCs in left anterior and left posterior superior temporal gyrus (STG), and may be due to higher activation in the left hemisphere in schizophrenia (Kuga et al., 2016; Agcaoglu et al., 2017).

In this paper, we present a spatial source phase analysis to evaluate spatial activation variability based on

resting-state complex-valued fMRI data. Results suggest that the spatial source phase has the potential to serve as a new brain imaging biomarker for brain disease diagnosis. However, several limitations to this study need to be mentioned. Firstly, we measured the spatial activation variability using resting-state fMRI data. It is also worth further study on whether the valuable conclusion can also be found in task-related fMRI data and how phase variation is modified by a variety of task paradigms. Secondly, independent vector analysis (IVA) is an effective approach for source separation and has been shown to perform better for preserving spatial activation variability across subjects (Michael et al., 2014; Gopal et al., 2015). This leads us to further explore the spatial source phase characteristic with IVA. Thirdly, we utilized the spatial source phase separately. Definition of a composite marker using both the magnitude and spatial source phase may also highlight more spatial differences than using the magnitude only. In addition, based on our findings that the spatial source phase has both intra- and inter- group differences (as shown in Figs. 7 and 8), this suggests that the classification of a single schizophrenia patient based on spatial source phase may be a useful direction. And finally, the specific mechanism of spatial source phase is still uncertain and therefore further study of the biophysiological understanding of the phase is a long-term research goal.

# Acknowledgments

This work was supported by National Natural Science Foundation of China under Grants 61871067, 61379012, 61671106, 61331019 and 81471742, NSF grants 1539067, 0840895 and 0715022, NIH grants R01MH104680, R01MH107354, R01EB005846 and 5P20GM103472, the Fundamental Research Funds for the Central Universities (China, DUT14RC(3)037), China Scholarship Council, and the Supercomputing Center of Dalian University of Technology.

# References


Abou, E. A., Starck, T. J., Nikkinen, J., Tervonen, O., & Kiviniemi, V. (2010). The effect of model order selection in group PICA. *Human Brain Mapping, 31*(8), 1207–1216. http://dx.doi.org/10.1002/hbm.20929.

Adalı, T., & Calhoun, V. D. (2007). Complex ICA of brain imaging data. *IEEE Signal Processing Magazine, 24*(5), 136–139. http://dx.doi.org/10.1109/SP.2007.904742.

Adrian D. W., Maitra R. and Rowe D. B. (2018). Complex-valued time series modeling for improved activation detection in fMRI studies. *Annals of Applied Statistics*, in press. https://doi.org/10.1214/17-AOAS1117.

Agcaoglu, O., Miller, R., Damaraju, E., Rashid, B., Bustillo, J., & Cetin, M. S., et al. (2017). Decreased hemispheric connectivity and decreased intra- and inter- hemisphere asymmetry of resting state functional network connectivity in schizophrenia. *Brain Imaging & Behavior* (4), 1–16. http://dx.doi.org/10.1007/ s11682-017-9718-7.

Allen, E. A., Erhardt, E. B., Damaraju, E., Gruner, W., Segall, J. M., & Silva, R. F., et al. (2011). A baseline for the multivariate comparison of resting-state networks. *Frontiers in Systems Neuroscience, 5*(2), 1–23. http://dx.doi.org/10.3389/fnsys.2011.00002.

Anderson, J. E., Wible, C. G., Mccarley, R. W., Jakab, M., Kasai K., & Shenton, M. E. (2002). An MRI study of temporal lobe abnormalities and negative symptoms in chronic schizophrenia. *Schizophrenia Research, 58*(2), 123–134. http://dx.doi.org/10.1016/S0920-9964(01)00372-3.

Arbabshirani, M. R., Havlicek, M., Kiehl, K. A., Pearlson, G. D., & Calhoun, V. D. (2013). Functional network connectivity during rest and task conditions: a comparative study. *Human Brain Mapping, 34*(11), 2959–2971. http://dx.doi.org/10.1002/hbm.22118.

Arja, S. K., Feng, Z., Chen, Z., Caprihan, A., Kiehl, K. A., & Adalı, T., et al. (2010). Changes in fMRI magnitude data and phase data observed in block-design and event-related tasks. *Neuroimage, 49*(4), 3149–3160. http://dx.doi.org/10.1016/j.neuroimage.2009.10.087.

Belliveau, J. W., Kennedy, D. N., Mckinstry, R. C., Buchbinder, B. R., Weisskoff, R. M., & Cohen, M. S., et al. (1991). Functional mapping of the human visual cortex by magnetic resonance imaging. *Science, 254*(5032), 716–719. http://dx.doi.org/10.1126/science.1948051.

Calhoun, V. D., & Adalı, T. (2012a). Analysis of complex-valued functional magnetic resonance imaging data: are we just going through a "phase"? *Bulletin of the Polish Academy of Sciences Technical Sciences, 60*(3), 371–418. http://dx.doi.org/10.2478/v10175-012-0050-5.

Calhoun, V. D., & Adalı, T. (2012b). Multi-subject independent component analysis of fMRI: A decade of intrinsic networks, default mode, and neurodiagnostic discovery. *IEEE Reviews in Biomedical Engineering, 5*, 60–73. http://dx.doi.org/10.1109/RBME.2012.2211076.

Calhoun, V. D., Adalı, T., Pearlson, G. D., Van Zijl, P. C. M., & Pekar, J. J. (2002). Independent component analysis of fMRI data in the complex domain. *Magnetic Resonance in Medicine, 48*(1), 180–192. http://dx.doi.org/10.1002/mrm.10202.

Calhoun, V. D., Eichele, T., & Pearlson, G. (2009). Functional brain networks in schizophrenia: a review. *Frontiers in Human Neuroscience, 3*(17), 1–12. http://dx.doi.org/10.3389/ neuro.09.017.2009.

Calhoun, V. D., Kiehl, K. A., Liddle, P. F., & Pearlson, G. D. (2004). Aberrant localization of synchronous hemodynamic activity in auditory cortex reliably characterizes schizophrenia. *Biological Psychiatry, 55*(8), 842–849. http://dx.doi.org/10.1016/j.biopsych.2004.01.011.

Calhoun, V. D., Maciejewski, P. K., Pearlson, G. D., & Kiehl, K. A. (2008). Temporal lobe and "default" hemodynamic brain modes discriminate between schizophrenia and bipolar disorder. *Human Brain Mapping, 29*(11), 1265–1275. http://dx.doi.org/10.1002/hbm.20463.

Castro, E., Gómez-Verdejo, V., Martínez-Ramón, M., Kiehl, K. A., & Calhoun, V. D. (2014). A multiple kernel learning approach to perform classification of groups from complex-valued fMRI data analysis: Application to schizophrenia. *Neuroimage, 87*(3), 1–17. http://dx.doi.org/10.1016/ j.neuroimage.2013. 10.065.

Chen, Z., & Calhoun, V. D. (2010). Magnitude and phase behavior of multiresolution bold signal. *Concepts in Magnetic Resonance Part B Magnetic Resonance Engineering, 37b*(3), 129–145. http://dx.doi.org/ 10.1002/cmr.b.20164.

Chen, Z., & Calhoun, V. D. (2016). T2* phase imaging and processing for brain functional magnetic susceptibility (χ) mapping. *Biomedical Physics & Engineering Express, 2*(2), 1–12. http://dx.doi.org/ 10.1088/ 2057-1976/2/2/025015.

Chen, Z., Caprihan, A., Damaraju, E., Rachakonda, S., & Calhoun, V. D. (2018). Functional brain connectivity in resting-state fMRI using phase and magnitude data. *Journal of Neuroscience Methods, 293*, 299–309. http://dx.doi.org/10.1016/j.jneumeth.2017.10.016.

Curtis, A. T., Hutchison, R. M., & Menon, R. S. (2014). Phase based venous suppression in resting-state bold GE-fMRI. *Neuroimage, 100*, 51–59. http://dx.doi.org/10.1016/ j.neuroimage.2014.05.079.

Efron, B., & Tibshirani R. J. (1993). *An Introduction to the Bootstrap.* New York, Chapman & Hall/CRC.

Fletcher, P., Mckenna, P. J., Friston, K. J., Frith, C. D., & Dolan, R. J. (1999). Abnormal cingulate modulation of fronto-temporal connectivity in schizophrenia. *Neuroimage, 9*(3), 337–342. http://dx.doi.org/10.1006/nimg.1998.0411.

Garrity, A. G., Pearlson, G. D., Mckiernan, K., Lloyd, D., Kiehl, K. A., & Calhoun, V. D. (2007). Aberrant 'default mode' functional connectivity in schizophrenia. *American Journal of Psychiatry, 164*(3), 450–457. http://dx.doi.org/10.1176/appi.ajp.164.3.450.

Gopal, S., Miller, R. L., Michael, A., Adalı, T., Cetin, M., & Rachakonda, S., et al. (2016). Spatial variance in resting fMRI networks of schizophrenia patients: an independent vector analysis. *Schizophrenia Bulletin, 42*(1), 152–160. http://dx.doi.org/10.1093/schbul/sbv085.

Grossman, M., Peelle, J. E., Smith, E. E., Mcmillan, C. T., Cook, P., & Powers, J., et al. (2013). Category-specific semantic memory: converging evidence from bold fmri and Alzheimer's disease. *Neuroimage, 68*, 263–274. http://dx.doi.org/10.1016/j.neuroimage.2012.11.057.

Hagberg, G., & Tuzzi, E. (2014). Phase variations in fMRI time series analysis: Friend or foe? *Advanced Brain Neuroimaging Topics in Health and Disease - Methods and Applications*. http://dx.doi.org/ 10.5772/31782.

Harrison, B. J., Yücel, M., Pujol, J., & Pantelis, C. (2007). Task-induced deactivation of midline cortical regions in schizophrenia assessed with fMRI. *Schizophrenia Research, 91*(1), 82-86. http://dx.doi.org/10.1016/j.schres.2006.12.027.

He, Y., Chen, Z., Gong, G., & Evans, A. (2009). Neuronal networks in Alzheimer's disease. *Neuroscientist, 15*(4), 333–350. http://dx.doi.org/10.1177/1073858409334423.

Hoogenraad, F. G., Reichenbach, J. R., Haacke, E. M., Lai, S., Kuppusamy, K., & Sprenger, M. (1998). In vivo measurement of changes in venous blood-oxygenation with high resolution functional MRI at 0.95

Tesla by measuring changes in susceptibility and velocity. *Magnetic Resonance Medicine, 39*(1), 97–107. http://dx.doi.org/10.1002/mrm.1910390116.

Jafri, M. J., Pearlson, G. D., Stevens M., & Calhoun V. D. (2008). A method for functional network connectivity among spatially independent resting-state components in schizophrenia. *Neuroimage, 39*(4), 1666–1681. https://doi.org/10.1016/j.neuroimage.2007.11.001.

Jeong, B., & Kubicki, M. (2010). Reduced task-related suppression during semantic repetition priming in schizophrenia. *Psychiatry Research: Neuroimaging, 181*(2), 114–120. http://dx.doi.org/10.1016/ j.pscychresns.2009.09.005.

Kuang, L. D., Lin, Q. H., Gong, X. F., Chen, Y. G., Cong, F., & Calhoun, V. D. (2017a). Model order effects on independent vector analysis applied to complex-valued fMRI data. In *International Symposium on Biomedical Imaging* (pp. 81–84). IEEE. http://dx.doi.org/10.1109 /ISBI.2017.7950473.

Kuang, L. D., Lin, Q. H., Gong, X. F., Cong, F., & Calhoun, V. D. (2017b). Post-ICA phase denoising for resting-state complex-valued fMRI data. In *IEEE International Conference on Acoustics, Speech and Signal Processing* (pp. 856–860). IEEE. http://dx.doi.org/10.1109/ ICASSP.2017.7952277.

Kuang, L. D., Lin, Q. H., Gong, X. F., Cong, F., Sui, J., & Calhoun, V. D. (2018). Model order effects on ICA of resting-state complex-valued fMRI data: application to schizophrenia. *Journal of Neuroscience Methods, 304*, 24–38. http://dx.doi.org/10.1016/j.jneumeth.2018. 02.013.

Kuga, H., Onitsuka, T., Hirano, Y., Nakamura, I., Oribe, N., & Mizuhara, H., et al. (2016). Increased bold signals elicited by high gamma auditory stimulation of the left auditory cortex in acute state schizophrenia. *Ebiomedicine, 12,* 143–149. http://dx.doi.org/10.1016/ j.ebiom.2016. 09.008.

Li, X. L., & Adalı, T. (2010). Complex independent component analysis by entropy bound minimization. *IEEE Transactions on Circuits & Systems I: Regular Papers, 57*(7), 1417–1430. http://dx.doi.org/ 10.1109/TCSI.2010.2046207.

Mannell, M. V., Franco, A. R., Calhoun, V. D., Cañive, J. M., Thoma, R. J., & Mayer, A. R. (2010). Resting state and task-induced deactivation: a methodological comparison in patients with schizophrenia and healthy controls. *Human Brain Mapping, 31*(3): 424–437. http://dx.doi.org/10.1002/hbm.20876.

McKeown, M. J., Makeig, S., Brown, G. G., Jung, T. P., Kindermann, S. S., & Bell, A. J., et al. (1998). Analysis of fMRI data by blind separation into independent spatial components. *Human Brain Mapping, 6*(3), 160-188. http://dx.doi.org/10.1002/(SICI)1097–0193.

Menon, R. S. (2002). Postacquisition suppression of large-vessel BOLD signals in high-resolution fMRI. *Magnetic Resonance in Medicine, 47*(1), 1–9. http://dx.doi.org/10.1002/ mrm.10041.

Michael, A. M., Anderson, M., Miller, R. L., Adalı, T., & Calhoun, V. D. (2014). Preserving subject variability in group fMRI analysis: performance evaluation of GICA vs. IVA. *Frontiers in Systems Neuroscience, 8*(106), 1–18. http://dx.doi.org/10.3389/fnsys.2014.00106.

Nencka, A. S., & Rowe, D. B. (2007). Reducing the unwanted draining vein BOLD contribution in fMRI with statistical post-processing methods. *Neuroimage, 37*(1), 177–188. http://dx.doi.org/10.1016/ j.neuroimage.2007.03.075.

Olabi, B., Ellisonwright, I., Mcintosh, A. M., Wood, S. J., Bullmore, E., & Lawrie, S. M. (2011). Are there progressive brain changes in schizophrenia? A meta-analysis of structural magnetic resonance imaging studies. *Biological Psychiatry, 70*(1), 88–96. http://dx.doi.org/ 10.1016/j.biopsych.2011.01.032.

Ogawa, S., Lee, T., Nayak, A. S., & Glynn, P. (1990). Oxygenation sensitive contrast in magnetic resonance image of rodent brain at high magnetic fields. *Magnetic Resonance in Medicine, 14*(1), 68–78. http://dx.doi.org/10.1002/mrm.1910140108.

Padmanabhan, J. L., Tandon, N., Haller, C. S., Mathew, I. T., Eack, S. M., & Clementz, B. A., et al. (2015). Correlations between brain structure and symptom dimensions of psychosis in schizophrenia, schizoaffective, and psychotic bipolar I disorders. *Schizophrenia Bulletin, 41*(1), 154–162. http:// dx.doi.org/ 10.1093/schbul/sbu075.

Pearlson, G. D., Barta, P. E., Powers, R. E., Menon, R. R., Richards, S. S., & Aylward, E. H., et al. (1997). Medial and superior temporal gyral volumes and cerebral asymmetry in schizophrenia versus bipolar disorder. *Biological Psychiatry, 41*(1), 1-14. https://doi.org/ 10.1016/ S0006-3223(96)00373-3.

Rodriguez, P. A., Calhoun, V. D., & Adalı, T. (2012). Denoising, phase ambiguity correction and visualization techniques for complex-valued ICA of group fMRI data. *Pattern Recognition, 45*(6), 2050–2063. http://dx.doi.org/10.1016/j.patcog.2011.04.033.

Rodriguez, P. A., Correa, N. M., Eichele, T., Calhoun, V. D., & Adalı, T. (2011): Quality map thresholding for denoising of complex-valued fMRI data and its application to ICA of fMRI. *Journal of Signal Processing Systems, 65*(3), 497–508. http://dx.doi.org/10.1007/s11265-010-0536-z.

Rowe, D. B., Nencka, A. S., & Hoffmann, R. G. (2007). Signal and noise of Fourier reconstructed fMRI data. *Journal of Neuroscience Methods, 159*(2), 361–369. http://dx.doi.org/10.1016/j.jneumeth.2006. 07.022.

Smith, S. M., Fox, P. T., Miller, K. L., Glahn, D. C., Fox, P. M., & Mackay, C. E., et al. (2009). Correspondence of the brain's functional architecture during activation and rest. *Proceedings of the National Academy of Sciences of the United States of America, 106*(31), 13040-13045. http://dx.doi.org/10.1073/pnas.0905267106.

Stippich, C. (2008). Clinical functional magnetic resonance imaging (fMRI). *Clinical Neuroradiology, 18*(1), 45–53. http://dx.doi.org/10.1007/s00062-008-8005-9.

Sui, J., Pearlson, G. D., Du, Y., Yu, Q., Jones, T. R., & Chen, J., et al, (2015). In search of multimodal neuroimaging biomarkers of cognitive deficits in schizophrenia. *Biological Psychiatry, 78*(11), 794–804. http://dx.doi.org/10.1016/j.biopsych.2015.02.017.

Sweet, R. A., Henteleff, R. A., Zhang, W., Sampson, A. R., & Lewis, D. A. (2008). Reduced dendritic spine density in auditory cortex of subjects with schizophrenia. *Neuropsychopharmacology, 34*(2), 374–389. http://dx.doi.org/10.1038/npp.2008.67.

Tomasi, D. G., & Caparelli, E. C. (2007). Macrovascular contribution in activation patterns of working memory. *Journal of Cerebral Blood Flow & Metabolism, 27*(1), 33–42. http://dx.doi.org/10.1038/ sj.jcbfm.9600314.

Whitfield-Gabrieli, S., Thermenos, H. W., Milanovic, S., Tsuang, M. T., Faraone, S. V., & McCarley, R. W., et al. (2009). Hyperactivity and hyperconnectivity of the default network in schizophrenia and in first-degree relatives of persons with schizophrenia. *Proceedings of the National Academy of Sciences of the United States of America, 106*(4), 1279–1284. http://dx.doi.org/10.1073/pnas.0809141106.

Yu, M. C., Lin, Q. H., Kuang, L. D., Gong, X. F., Cong, F., & Calhoun, V. D. (2015). ICA of full complex-valued fMRI data using phase information of spatial maps. *Journal of Neuroscience Methods, 249*, 75–91. http://dx.doi.org/10.1016/j.jneumeth.2015.03.036.

# Tables

**Table I.** The proposed method for spatial source phase analysis.

**Input:** Complex-valued fMRI data of $\mathbf{X}^k \in \mathbb{C}^{T \times V}$ ($k = 1, \ldots, K$), spatial reference network $\mathbf{s}_{\text{ref}}$, number of components *N*, and number of runs *R*

1. Perform the complex-valued ICA algorithm EBM on $\mathbf{X}^k$, and obtain TC and SM estimates for *N* components. Repeat *R* times.
2. Select the TC and SM estimates $\mathbf{a}_r^k$ and $\mathbf{s}_r^k$ ($r = 1, \ldots, R$) for a component of interest from the *N* components of each run using $\mathbf{s}_{\text{ref}}$ and criterion defined in Eq. (1).
3. Correct $\mathbf{s}_r^k$ to obtain $\underline{\mathbf{s}}_r^k$ using Eqs. (2) and (3).
4. Construct the single-subject binary mask $\mathbf{b}_r^k$ using Eq. (4) and obtain the denoised single-subject SM estimate $\underline{\mathbf{s}}_{r,*}^k$ using Eq. (5).
5. Select the best run $r^*$ from $\underline{\mathbf{s}}_{r,*}^k$ among *R* runs using Eq. (6) and (7).
6. Construct the group mask $\tilde{\mathbf{b}}$ using Eq. (8), and mask $\underline{\mathbf{s}}_{r^*}^k$ with $\tilde{\mathbf{b}}$ to get $\underline{\mathbf{s}}_*^k$ using Eq. (9).
7. Construct the spatial source phase vectors $\boldsymbol{\varphi}_i^{\text{SZ}}$ and $\boldsymbol{\varphi}_i^{\text{HC}}$ ($i = 1, \cdots, M$) using the spatial source phase values in $\underline{\mathbf{s}}_*^1, \ldots, \underline{\mathbf{s}}_*^K$.
8. Perform the homogeneity of variance test (voxel-wise *F*-test) with and without FDR correction on $\boldsymbol{\varphi}_i^{\text{SZ}}$ and $\boldsymbol{\varphi}_i^{\text{HC}}$ to get the difference variance map of SZ-HC $\mathbf{d}_{\text{SZ-HC}}^*$ using Eq. (10).
9. Record the number of nonzero elements $m_*$ in $\mathbf{d}_{\text{SZ-HC}}^*$, and calculate the variance difference indexes $q^*$ and $q_{\text{SZ-HC}}^*$ using Eq. (11).

**Output:** The difference variance map of SZ-HC $\mathbf{d}_{\text{SZ-HC}}^*$, the number of significant voxels $m_*$, and the variance difference indexes $q^*$ and $q_{\text{SZ-HC}}^*$.

**Table II.** The proposed validation method.

| |
|---|
| **Input:** Spatial source phase vector $\boldsymbol{\varphi}_i^{\mathrm{SZ}} \in \mathbb{R}^{K_1}$ and $\boldsymbol{\varphi}_i^{\mathrm{HC}} \in \mathbb{R}^{K_2}$ ($i = 1, \cdots, M$), number of subjects $K'$ in each sub-group, number of runs $L$ |
| **1.** Construct sub-groups G1 and G2 by randomly selecting $K'$ subjects from (1) SZs, (2) HCs, and (3) SZs and HCs, respectively. Repeat $L$ times to form $L$ trials. |
| **2.** Construct the spatial source phase vectors $\boldsymbol{\varphi}_i^{[l,\mathrm{G1}]}$ and $\boldsymbol{\varphi}_i^{[l,\mathrm{G2}]}$ for each trial, $l = 1, \cdots, L$. |
| **3.** Perform the voxel-wise $F$-test with and without FDR correction on $\boldsymbol{\varphi}_i^{[l,\mathrm{G1}]}$ and $\boldsymbol{\varphi}_i^{[l,\mathrm{G2}]}$ to get the difference variance map of G1-G2 $\mathbf{d}_{\mathrm{G1\text{-}G2}}^{[l,*]}$ using Eq. (12) for each trial. |
| **4.** Calculate $m_*^{\mathrm{G}}$ by averaging $m_*^l$ across $L$ trials for (1) intra-SZ, (2) intra-HC and (3) inter group differences, respectively, where $m_*^l$ denotes the number of nonzero elements in $\mathbf{d}_{\mathrm{G1\text{-}G2}}^{[l,*]}$. |
| **5.** Calculate the mean variance difference indexes $\bar{q}_{\mathrm{G}}^*$ and $q_{\mathrm{G1\text{-}G2}}^*$ for (1) intra-SZ, (2) intra-HC and (3) inter-group differences using Eq. (13), respectively. |
| **Output:** The number of significant voxels $m_*^{\mathrm{G}}$ and the mean variance difference indexes $\bar{q}_{\mathrm{G}}^*$ and $q_{\mathrm{G1\text{-}G2}}^*$ for intra-SZ, intra-HC and inter-group differences. |

**Table III.** Variance difference validation using bootstrap sampling. Unsigned values $q^*$ are used in the calculation of *p*-values using the BCa method and computation of mean and standard deviations for $q^*_{\text{SZ-HC}}$ from relabeled data. The values of $m_*$ are provided together with $q^*_{\text{SZ-HC}}$ for determining whether the difference is significant. The sub-networks ACC and AL satisfy both $m_* > 200$ and $|q^*_{\text{SZ-HC}}| \geq 0.8$.

| | | $m_*$ (all SZ-HC) | $q^*_{\text{SZ-HC}}$ (all SZ-HC) | $m_*$ (relabeled SZ-HC for 1000 runs) | $q^*$ (relabeled SZ-HC for1000 runs) | *p*-values **(**BCa method**)** |
|---|---|---|---|---|---|---|
| without FDR | PCC | 1356 | -0.505 | 1652±153 | 0.531±0.156 | 0.843 |
| | IPL | 625 | 0.763 | 903±94 | 0.646±0.124 | 0.003 |
| | **ACC** | **851** | **1.000** | **898±177** | **0.974±0.033** | **$7.159\times10^{-36}$** |
| | **AL** | **1092** | **0.963** | **1309±172** | **0.882±0.094** | **$7.732\times10^{-10}$** |
| | AR | 751 | 0.762 | 1095±125 | 0.701±0.129 | 0.029 |
| with FDR | PCC | 1317 | -0.509 | 1651±154 | 0.531±0.156 | 0.808 |
| | IPL | 601 | 0.780 | 902±95 | 0.647±0.124 | 0.001 |
| | **ACC** | **826** | **1.000** | **897±178** | **0.974±0.033** | **$5.825\times10^{-36}$** |
| | **AL** | **981** | **0.973** | **1304±179** | **0.883±0.094** | **$5.023\times10^{-13}$** |
| | AR | 660 | 0.759 | 1090±132 | 0.702±0.129 | 0.032 |

# Figures

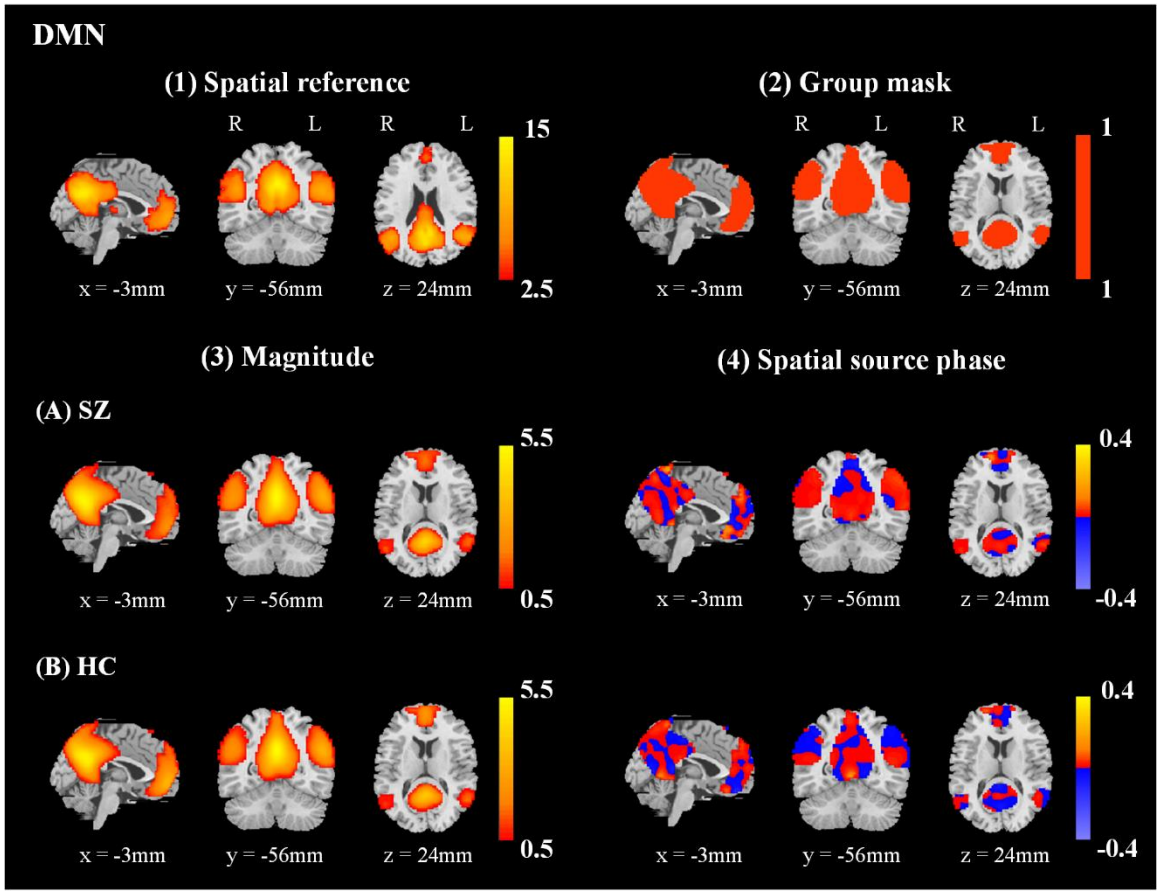


**Figure 1.** Comparison of maps for the DMN. (1) Spatial reference detected in Smith et al. (2009). (2) Group mask for all subjects. (3) Group magnitude maps for (A) SZs and (B) HCs. (4) Group spatial source phase maps for (A) SZs and (B) HCs. The group spatial source phase maps exhibit more spatial differences than the group magnitude maps in the DMN.

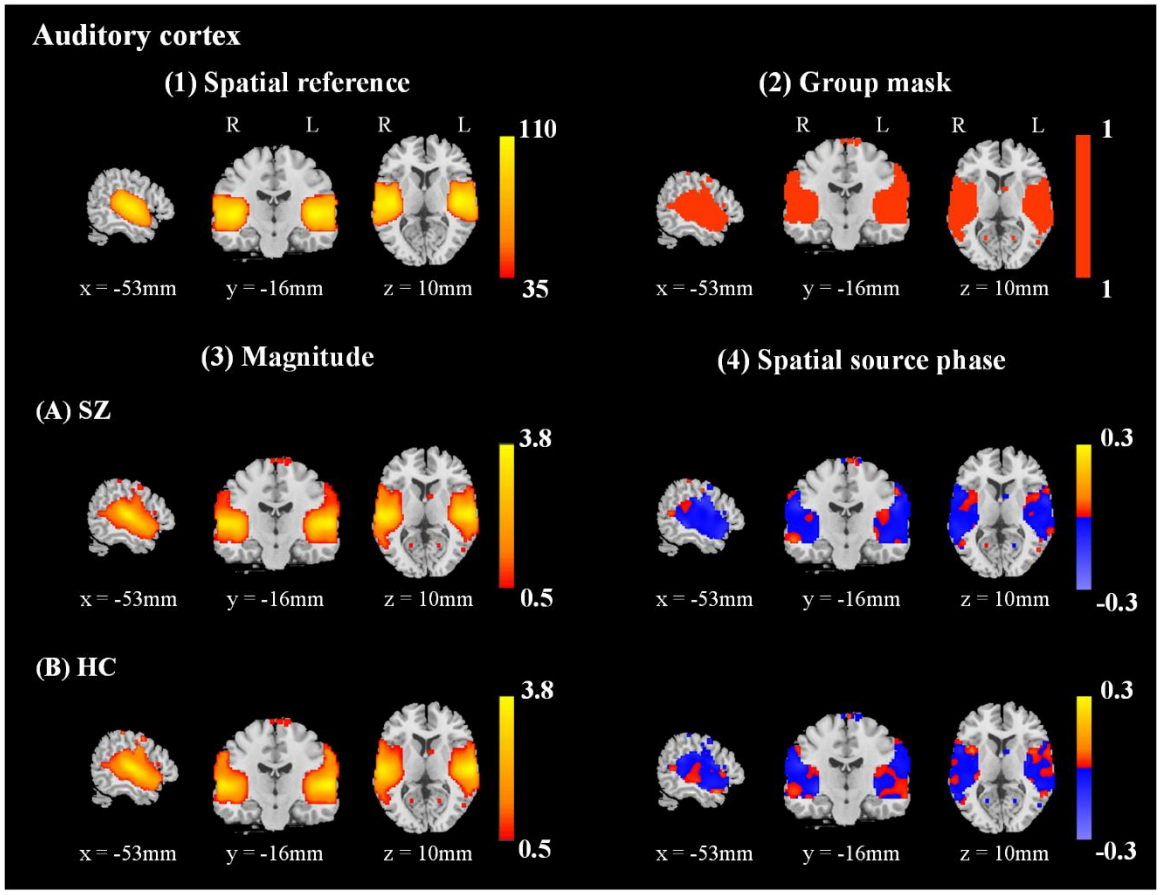


**Figure 2.** Comparison of maps for the auditory cortex. (1) Spatial reference detected in Allen et al. (2011). (2) Group mask for all subjects. (3) Group magnitude maps for (A) SZs and (B) HCs. (4) Group spatial source phase maps for (A) SZs and (B) HCs. The group spatial source phase maps exhibit more spatial differences than the group magnitude maps in the auditory cortex.

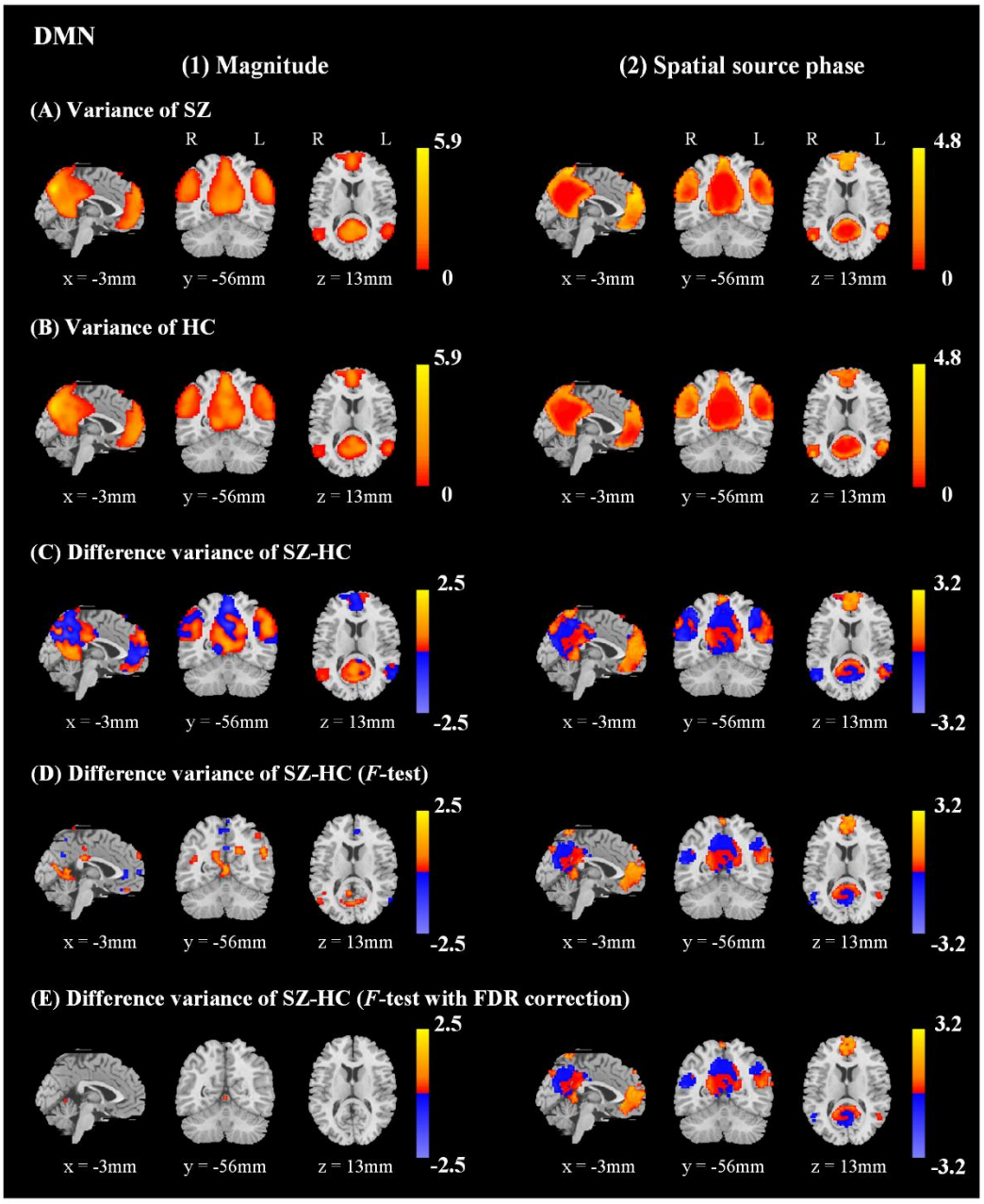


**Figure 3.** Comparison of the DMN difference variance maps of SZ-HC from (1) magnitude and (2) spatial source phase. (A) Variance maps of SZs. (B) Variance maps of HCs. (C) Difference variance maps of SZ-HC. (D) Difference variance maps of SZ-HC with voxel-wise *F*-test at $p < 0.05$. (E) Difference variance maps of SZ-HC with voxel-wise *F*-test at $p < 0.05$ (FDR corrected). More differences in the spatial source phase maps successfully survived the voxel-wise *F*-test (with and without FDR correction) than the magnitude maps.

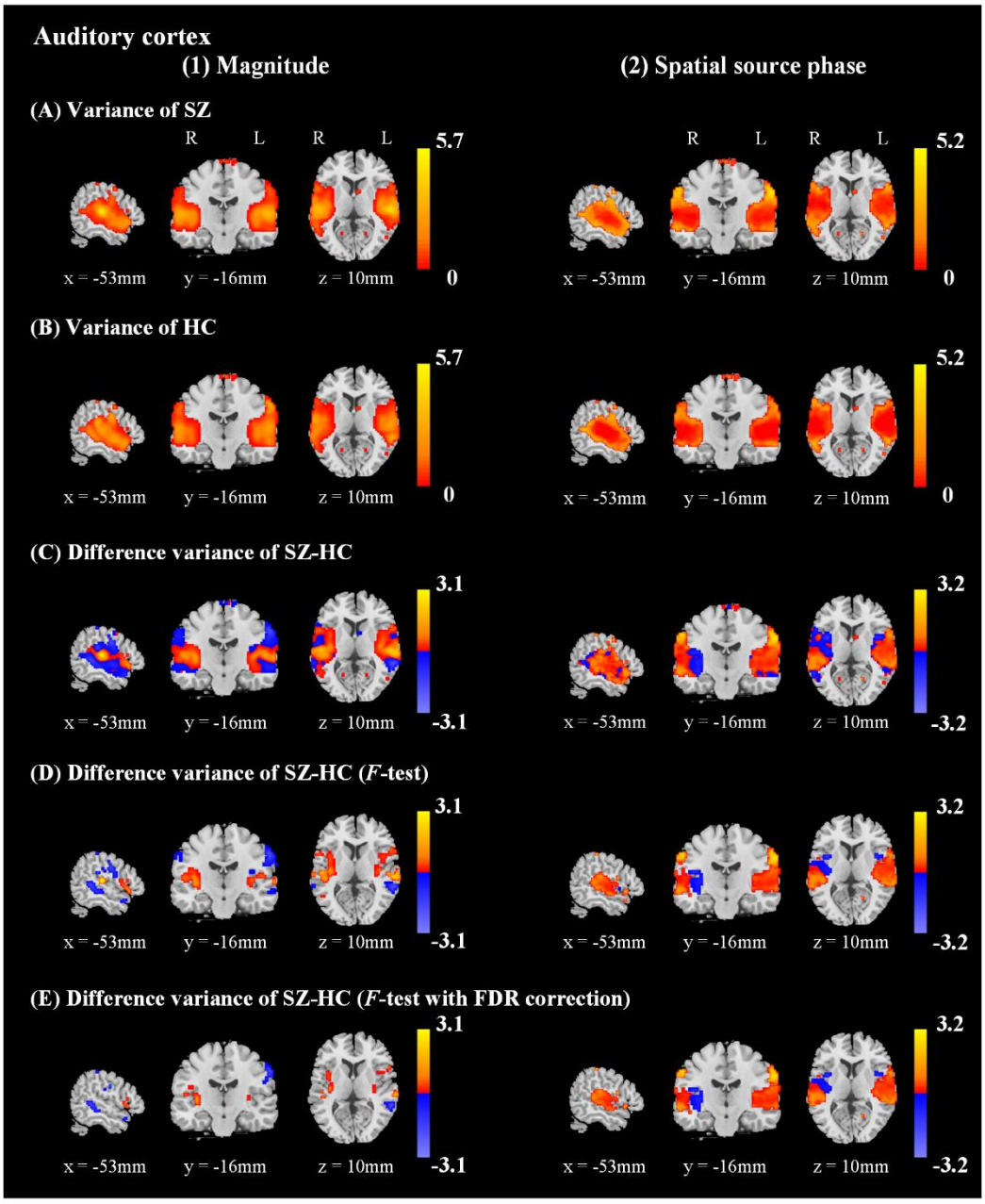


**Figure 4.** Comparison of the auditory difference variance maps of SZ-HC from (1) magnitude and (2) spatial source phase. (A) Variance maps of SZs. (B) Variance maps of HCs. (C) Difference variance maps of SZ-HC. (D) Difference variance maps of SZ-HC with voxel-wise *F*-test at $p < 0.05$. (E) Difference variance maps of SZ-HC with voxel-wise *F*-test at $p < 0.05$ (FDR corrected). More differences in the spatial source phase maps successfully survived the voxel-wise *F*-test (with and without FDR correction) than the magnitude maps.

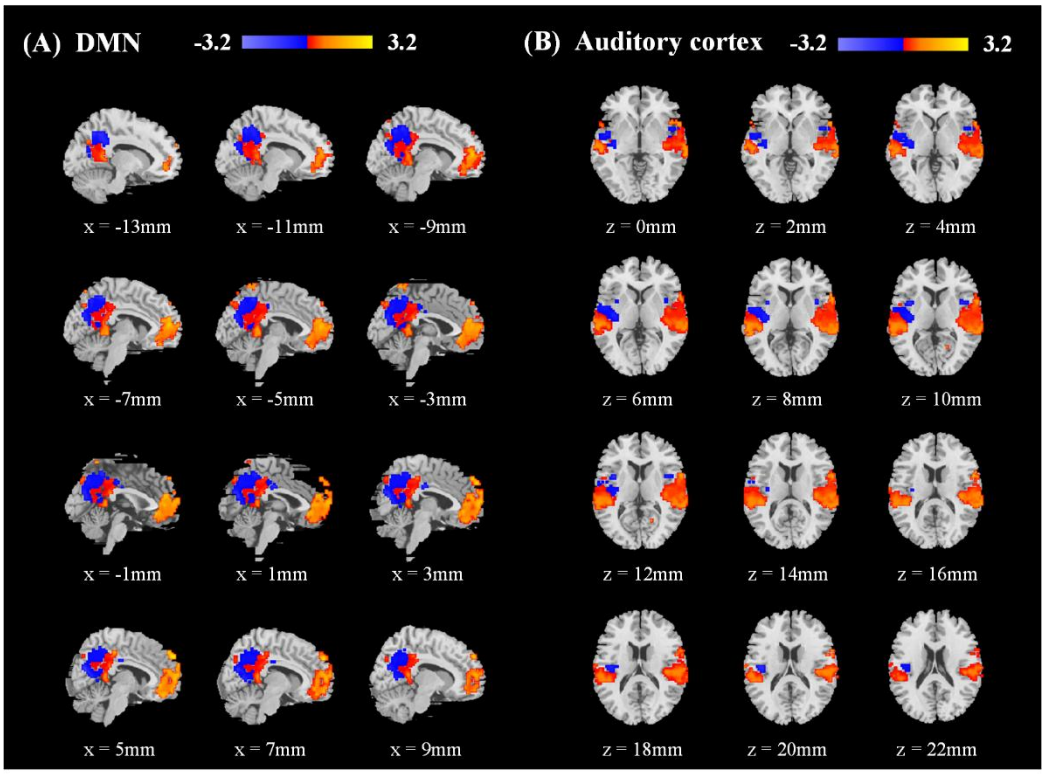


**Figure 5.** Multiple slices, centered with the specific slices shown in Figs. 3(E) and 4(E), in difference variance maps of SZ-HC (*F*-test with FDR correction) detected from spatial source phase. (A) DMN. (B) Auditory cortex. Increased variance clusters in ACC and AL are observed.

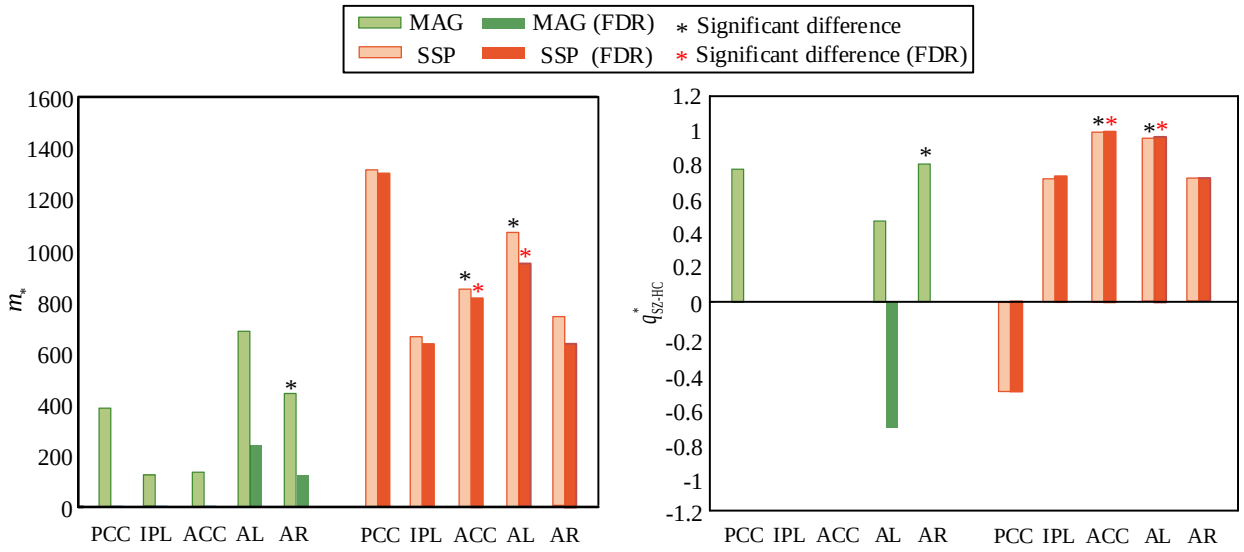


**Figure 6.** Comparison of SZ-HC differences in magnitude and spatial source phase in terms of the number of significant voxels $m_*$ survived the voxel-wise *F*-test at $p < 0.05$ (with and without FDR correction of 0.05) and the difference variance index $q^*_{SZ\text{-}HC}$ for sub-networks of DMN and auditory cortex. $q^*_{SZ\text{-}HC}$ was calculated only when $m_* > 200$ with the purpose of taking more voxels into the computation. The difference with $m_* > 200$ and $|q^*_{SZ\text{-}HC}| \geq 0.8$ is regarded as a signicant difference (*). More significant voxels were detected by the spatial source phase than the magnitude for all sub-networks, and more voxels in the spatial source phase maps passed FDR correction than the magnitude maps. Spatial phase maps detected signifiant differences with FDR correction in ACC and AL.

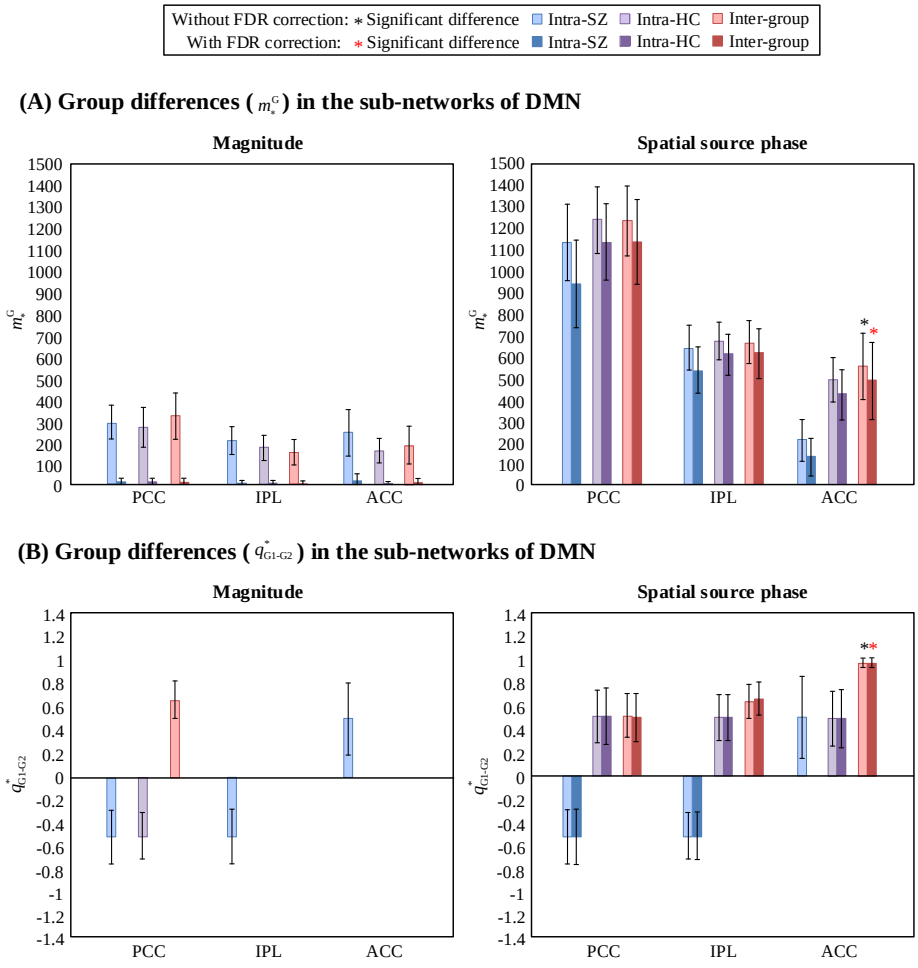


**Figure 7.** Comparison of intra-SZ, intra-HC and inter-group differences survived voxel-wise *F*-test at $p < 0.05$ (with and without FDR correction of 0.05) in the sub-networks of DMN for magnitude maps (left) and spatial source phase maps (right). (A) The number of significant voxels ( $m_*^G$ ). (B) The mean variance difference index $q^*_{G1\text{-}G2}$ (calculated only when $m_*^G > 200$ ). Note that standard deviations of $m_*^G$ and $q^*_{G1\text{-}G2}$ are also shown. The spatial source phase is more sensitive to the inter-group differences and highlights a key region ACC which is consistent with the regions showing significant differences between SZs and HCs detected in Fletcher et al. (1999).

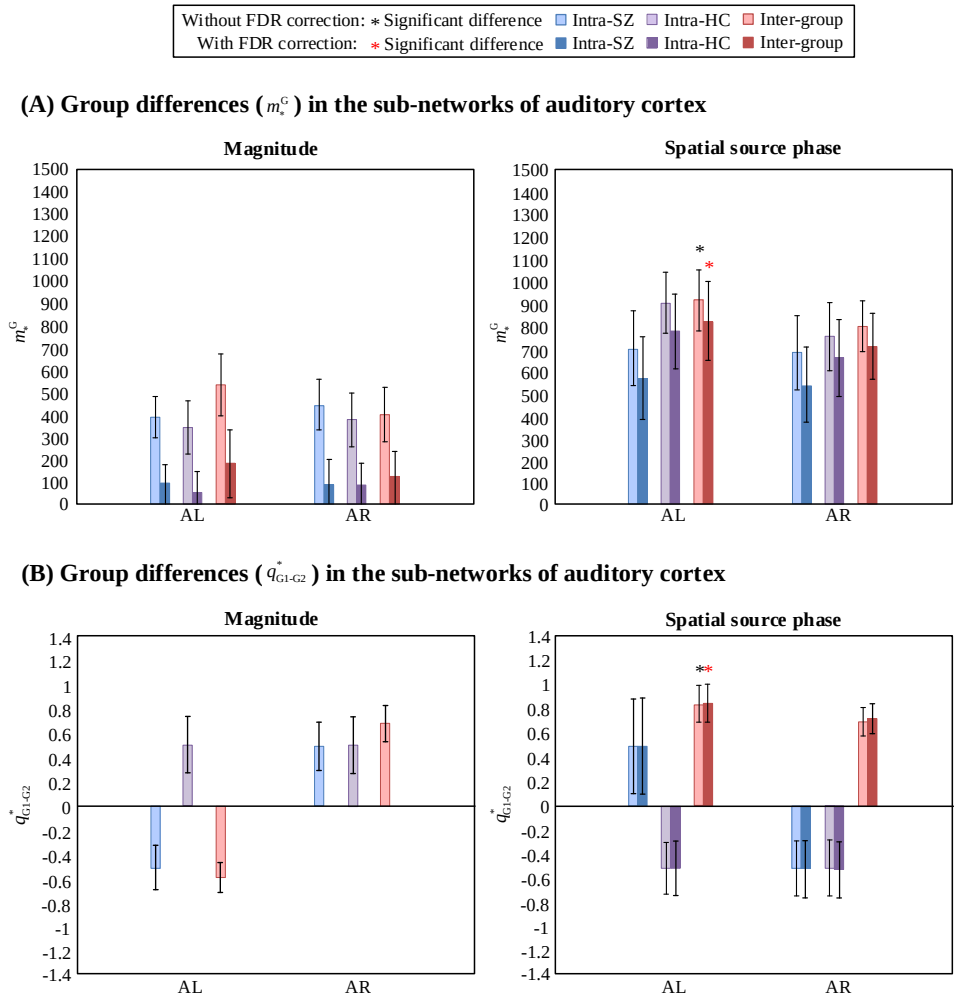


**Figure 8.** Comparison of intra-SZ, intra-HC and inter-group differences survived voxel-wise *F*-test at $p < 0.05$ (with and without FDR correction of 0.05) in the sub-networks of auditory cortex for magnitude maps (left) and spatial source phase maps (right). (A) The number of significant voxels ( $m_*^G$ ). (B) The mean variance difference index $q^*_{G1\text{-}G2}$ (calculated only when $m_*^G > 200$ ). Note that standard deviations of $m_*^G$ and $q^*_{G1\text{-}G2}$ are also shown. The spatial source phase is more sensitive to the inter-group differences and highlights a key region AL which is consistent with the results in Pearlson et al. (1997) from structural MRI data showing differences between SZs and HCs in left anterior and left posterior superior temporal gyrus.